



FORWARD AND INVERSE MODELING OF THE EMISSION AND TRANSMISSION SPECTRUM OF GJ 436B: INVESTIGATING METAL ENRICHMENT, TIDAL HEATING, AND CLOUDS

CAROLINE V. MORLEY^{1,2,7}, HEATHER KNUTSON³, MICHAEL LINE⁴, JONATHAN J. FORTNEY², DANIEL THORNGREN⁵,
MARK S. MARLEY⁶, DILLON TEAL², AND ROXANA LUPU⁶

¹Department of Astronomy, Harvard University, 60 Garden Street, Cambridge, MA 02138, USA; caroline.morley@cfa.harvard.edu

²Department of Astronomy and Astrophysics, University of California, 1156 High Street, Santa Cruz, CA 95064, USA

³Division of Geological and Planetary Sciences, California Institute of Technology, 1200 East California Boulevard, Pasadena, CA 91125, USA

⁴School of Earth and Space Exploration, Arizona State University, 781 South Terrace Road, Tempe, AZ 85281, USA

⁵Department of Physics, University of California, 1156 High Street, Santa Cruz, CA 95064, USA

⁶NASA Ames Research Center, Moffett Field, CA 94035, USA

Received 2016 June 29; revised 2016 December 13; accepted 2016 December 14; published 2017 January 26

ABSTRACT

The Neptune-mass GJ 436b is one of the most studied transiting exoplanets with repeated measurements of its thermal emission and transmission spectra. We build on previous studies to answer outstanding questions about this planet, including its potentially high metallicity and tidal heating of its interior. We present new observations of GJ 436b’s thermal emission at 3.6 and 4.5 μm , which reduce uncertainties in estimates of GJ 436b’s flux at those wavelengths and demonstrate consistency between *Spitzer* observations spanning more than 7 yr. We analyze the *Spitzer* thermal emission photometry and *Hubble* WFC3 transmission spectrum. We use a dual-pronged modeling approach of both self-consistent and retrieval models. We vary the metallicity, intrinsic luminosity from tidal heating, disequilibrium chemistry, and heat redistribution. We also study clouds and photochemical hazes, but do not find strong evidence for either. The self-consistent and retrieval models combine to suggest that GJ 436b has a high atmospheric metallicity, with best fits at or above several hundred times solar metallicity, tidal heating warming its interior with best-fit intrinsic effective temperatures around 300–350 K, and disequilibrium chemistry. High metal enrichments ($>600\times$ solar) occur from the accretion of rocky, rather than icy, material. Assuming the interior temperature $T_{\text{int}} \sim 300\text{--}350$ K, we find a dissipation factor $Q' \sim 2 \times 10^5\text{--}10^6$, larger than Neptune’s Q' , implying a long tidal circularization timescale for the orbit. We suggest that Neptune-mass planets may be more diverse than imagined, with metal enhancements spanning several orders of magnitude, to perhaps over $1000\times$ solar metallicity. High-fidelity observations with instruments like the *James Webb Space Telescope* will be critical for characterizing this diversity.

Key words: planets and satellites: atmospheres – planets and satellites: composition – planets and satellites: gaseous planets

1. INTRODUCTION

Determining the compositions of exoplanets ranging from Earth mass to Jupiter mass in different environments is a key goal of exoplanetary research. Planetary compositions are shaped by the details of planet formation and altered by atmospheric physics and chemistry. Over a decade after its discovery by Butler et al. (2004), GJ 436b remains the planet in its Neptune-mass class for which we have obtained the most detailed observations of its atmosphere.

GJ 436b was discovered to transit by Gillon et al. (2007b) and, as the smallest transiting planet in 2007 and a favorable target for observations, immediately became a target for atmospheric characterization studies with the *Spitzer Space Telescope* and *Hubble Space Telescope* (*HST*). It remains one of the most favorable and interesting targets for follow-up spectroscopic studies: to date a total of 18 secondary eclipses and eight transits have been observed with *Spitzer*, along with seven transits with *HST* (Deming et al. 2007; Demory et al. 2007; Gillon et al. 2007a; Stevenson et al. 2010; Beaulieu et al. 2011; Knutson et al. 2011, 2014a).

The atmosphere of GJ 436b has been a perennial challenge to understand. Previous observations and modeling efforts, which we describe below, have suggested high-metallicity

compositions with strong vertical mixing. Many of these conclusions rest on the robustness of the *Spitzer* 3.6 and 4.5 μm eclipses. Here, we move forward to study this planet using both its thermal emission photometry and its transmission spectrum, adding three new eclipse observations at these two wavelengths and analyzing the data set with a powerful dual-pronged approach of self-consistent and retrieval modeling.

1.1. Observations and Interpretation of Thermal Emission

Secondary eclipse measurements allow us to infer the planet’s brightness, and therefore temperature, as a function of wavelength when the planet passes behind the host star. A planet will appear fainter, and therefore create a shallower occultation, at wavelengths of strong absorption features, and it will appear brighter at wavelengths of emission features.

The first secondary eclipse measurements of GJ 436b were observed at 8 μm , while *Spitzer* was still operating cryogenically (Deming et al. 2007; Demory et al. 2007). These observations revealed that GJ 436b has a high eccentricity, ~ 0.15 , which, given predicted tidal circularization timescales, suggests the presence of a companion and of potential tidal heating (Ribas et al. 2008; Batygin et al. 2009).

With an equilibrium temperature around 700–800 K, GJ 436b is cool enough that models assuming thermochemical equilibrium predict high CH_4 abundance and low CO and CO_2

⁷ NASA Sagan Fellow.

abundance, which would result in a deeper occultation at $4.5\ \mu\text{m}$ than $3.6\ \mu\text{m}$. However, when Stevenson et al. (2010) published the first multiwavelength thermal emission spectrum of GJ 436b, measuring photometric points at 3.6, 4.5, 5.8, 8.0, 16, and $24\ \mu\text{m}$, they found that its occultation was deeper at $3.6\ \mu\text{m}$ and shallower at $4.5\ \mu\text{m}$ and suggested methane depletion due to photodissociation as an explanation. Additional studies have reanalyzed these observations and observed additional secondary eclipses (Knutson et al. 2011; Lanotte et al. 2014). In particular, the analysis by Lanotte et al. (2014) revealed a significantly shallower $3.6\ \mu\text{m}$ eclipse and somewhat shallower $8.0\ \mu\text{m}$ eclipse; no detailed atmospheric studies have been carried out since these revisions.

From the time of the initial observations of GJ 436b's thermal emission, it has been a major challenge to find self-consistent models that adequately explain the data. Madhusudhan & Seager (2011) found, using retrieval algorithms, that the atmosphere is best fit by an atmosphere rich in CO and CO_2 and depleted in CH_4 . Line et al. (2011) used disequilibrium chemical models including the effect of photochemistry, but found that they were not able to reproduce the low observed methane abundance. Moses et al. (2013) found that high metallicities ($230\text{--}1000\times$ solar) favor the high CO and CO_2 abundances inferred from the observations. Hu et al. (2015) explored scenarios in which the planet might be depleted in hydrogen but retain its helium, similarly increasing the CO and CO_2 abundances while decreasing the CH_4 abundance. Agúndez et al. (2014), noting the high eccentricity of GJ 436b, studied the effect of tidal heating deep in the atmosphere on the chemistry and found that significant tidal heating and high metallicities fit the observed photometry best.

1.2. Observations and Interpretation of Transmission Spectrum

Wavelength-dependent observations of the transit depth of GJ 436b allow us to probe the composition of GJ 436b's day-night terminator. At wavelengths with strong absorption features, the planet will occult a larger area of the star, resulting in a deeper transit depth. Pont et al. (2009) observed the transmission spectrum of GJ 436b from 1.1 to $1.9\ \mu\text{m}$ with NICMOS on *HST* but, due to systematic effects, were unable to achieve high enough precision to detect the predicted water vapor feature. Beaulieu et al. (2011) presented transit measurements in *Spitzer's* 3.6, 4.5, and $8.0\ \mu\text{m}$ filters that showed higher transit depths at 3.6 and $8.0\ \mu\text{m}$ than at $4.5\ \mu\text{m}$, indicating strong methane absorption. Knutson et al. (2011) analyzed the same data and suggested that variable stellar activity caused the observed transit depth at $3.6\ \mu\text{m}$ to vary between epochs. However, these data were reanalyzed again by Lanotte et al. (2014) and Morello et al. (2015) with new techniques, which both found that the transit depths were constant in the different bandpasses and remained constant between epochs of observations.

More recently, Knutson et al. (2014a) used WFC3 on *HST* to measure the transmission spectrum from 1.1 to $1.7\ \mu\text{m}$. Like Pont et al. (2009), they do not detect a water vapor feature, but with their higher signal-to-noise ratio (S/N) spectrum they are able to rule out a cloud-free H/He-dominated atmosphere to high confidence (48σ). The spectrum is consistent with a high cloud at pressures of ~ 1 mbar, or an H/He-poor (3% H/He by mass, $1900\times$ solar) atmospheric composition.

1.3. A Third Body in the GJ 436 System?

Because the tidal circularization timescales are predicted to be shorter than the age of the star, the nonzero eccentricity of GJ 436b has suggested that it may have at least one companion in the system; however, a number of searches for additional planets did not find additional bodies (Deming et al. 2007; Demory et al. 2007; Maness et al. 2007; Alonso et al. 2008; Ribas et al. 2008; Cáceres et al. 2009; Ballard et al. 2010a, 2010b; Beust et al. 2012). Stevenson et al. (2012) announced the detection of two candidate sub-Earth-sized planets in the system, but later work by Lanotte et al. (2014) did not find any evidence of these candidate companions.

1.4. The Need for an Additional Atmospheric Study

Here, we build on this extensive history of both observations and modeling for this enigmatic warm Neptune to answer the still-outstanding questions about this planet. Do the revisions in the eclipse points from Lanotte et al. (2014) change the inferred composition? Is it truly ultrahigh ($>300\times$ solar) metallicity? What atmospheric physics must be present for a Neptune-mass planet to have the observed spectra and inferred atmospheric composition?

To these ends, we present an additional three secondary eclipse observations (one at $3.6\ \mu\text{m}$, two at $4.5\ \mu\text{m}$), demonstrating the robustness of these observations with modern *Spitzer* observational and analysis techniques. We study both the thermal emission and transmission spectra of GJ 436b in tandem, including the published data set of *Spitzer* photometry spanning from 3.6 to $16\ \mu\text{m}$ and the transmission spectrum from *HST*/WFC3. Unlike most previous studies, we investigate whether including clouds or hazes in GJ 436b's atmosphere can match both sets of observations for Neptune-like compositions ($50\text{--}300\times$ solar), without invoking ultrahigh-metallicity ($>1000\times$ solar) compositions. We combine our self-consistent treatment with results from chemically consistent retrievals that do not include clouds and show that H/He-poor atmospheric compositions with tidal heating provide the most precise fit to GJ 436b's thermal emission spectrum, while also fitting the transmission spectrum.

1.4.1. Format of This Work

In Section 2 we describe the observations and data analysis. In Section 3 we describe the modeling tools used to simulate the observations, including both self-consistent and retrieval models. In Section 4.2 we compare the data to self-consistent models; in Section 4.3 we use retrieval algorithms to retrieve chemical abundances and the pressure-temperature (P-T) profile and compare these results with the results from self-consistent modeling.

2. OBSERVATIONS AND DATA ANALYSIS

2.1. Photometry and Instrumental Model

These observations were obtained in the 3.6 and $4.5\ \mu\text{m}$ bandpasses using the Infra-Red Array Camera (IRAC) on the *Spitzer Space Telescope*. In this paper we present three new secondary eclipse observations of this planet, including a $3.6\ \mu\text{m}$ observation obtained on UT 2014 July 29 and two $4.5\ \mu\text{m}$ observations obtained on UT 2014 August 11 and UT 2015 February 25, respectively, as part of *Spitzer* program 50056 (PI: H. Knutson). We also reexamine three archival

Table 1
Spitzer Observation Details

λ (μm)	UT Start Date	Length (hr)	$n_{\text{img}}^{\text{a}}$	t_{int} (s) ^b	$t_{\text{trim}}^{\text{c}}$	$n_{\text{bin}}^{\text{c}}$	$r_{\text{pos}}^{\text{c}}$	$r_{\text{phot}}^{\text{c}}$	Bkd (%) ^d
3.6	2008 Jan 30	5.9	163,200	0.1	1.0	192	3.0	2.8	0.05
3.6	2014 Jul 29	4.5	122,112	0.1	1.0	128	2.0	2.5	0.25
4.5	2008 Feb 02	5.9	49,920	0.4	3.0	32	2.0	2.9	0.09
4.5	2011 Jan 24	6.1	51,712	0.4	2.0	32	2.0	4.5	0.38
4.5	2014 Aug 11	4.5	122,112	0.1	0.5	128	2.0	2.7	0.11
4.5	2015 Feb 25	4.5	122,112	0.1	0.5	128	2.0	2.8	0.12

Notes.

^a Total number of images.

^b Integration time.

^c t_{trim} is the amount of time in hours trimmed from the start of each time series, n_{bin} is the bin size used in the photometric fits, r_{pos} is the radius of the aperture used to determine the position of the star on the array, and r_{phot} is the radius of the photometric aperture in pixels.

^d Sky background contribution to the total flux for the selected aperture.

eclipse observations including a 3.6 μm eclipse from UT 2008 January 30, as well as 4.5 μm eclipses from UT 2008 February 2 and UT 2011 January 24 (Stevenson et al. 2010, 2012; Lanotte et al. 2014). Eclipses from 2008 were observed during *Spitzer*'s cryogenic mission, while the remaining eclipses were observed during the extended warm mission. All eclipses were observed in subarray mode, with integration times and observation durations given in Table 1. Our new 2014–2015 observations included a now-standard 30-minute peak-up pointing observation prior to the start of our science observations (Ballard et al. 2014).⁸ This adjustment corrects the initial telescope pointing in order to place the star near the center of the pixel, where the effect of intrapixel sensitivity variations is minimized.

We utilize BCD image files for our photometric analysis and extract BJD_{UTC} mid-exposure times using the information in the image headers. The sky background for each 32×32 pixel image is calculated by excluding a circular region with a radius of 12 pixels centered on the star, taking all of the remaining pixels and trimming outliers greater than three standard deviations away from the median, and then fitting a Gaussian function to a histogram of the remaining pixels. We calculate the flux-weighted centroid position of the star on the array and derive the corresponding total flux in a circular aperture for each individual image as described in previous studies (e.g., Lewis et al. 2013; Deming et al. 2015; Kammer et al. 2015). We consider both fixed and time-varying photometric aperture sizes in our fits but find that in all cases we obtain a lower rms and reduced levels of time-correlated (“red”) noise in our best-fit residuals using fixed apertures, in good agreement with the conclusions of Lanotte et al. (2014). We consider apertures with radii ranging between 2.0 and 5.0 pixels, where we step in increments of 0.1 pixels between 2.0 and 3.0 pixels and in 0.5 pixel increments for larger radii.

The sensitivity of individual 3.6 and 4.5 μm IRAC pixels varies from the center to the edge; when combined with short-term telescope pointing oscillations, this produces variations in the raw stellar fluxes plotted in Figure 1. We correct for this effect using the pixel-level decorrelation (PLD) method (Deming et al. 2015), which produces results that are comparable or superior to those from a simple polynomial decorrelation or pixel-mapping method for light curves with durations of less than 10 hr (for a discussion of the PLD

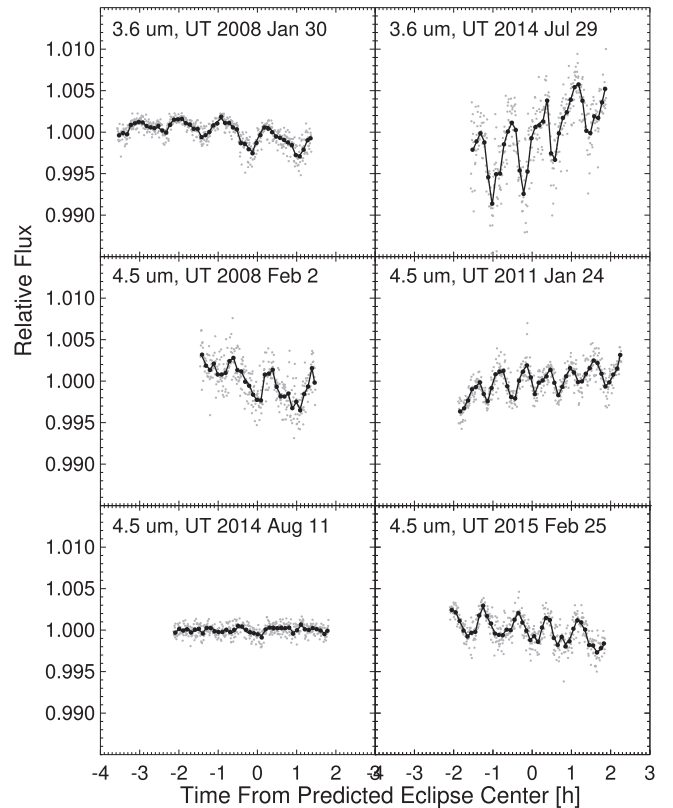


Figure 1. Raw *Spitzer* 3.6 and 4.5 μm photometry as a function of time from the center-of eclipse phase reported in Knutson et al. (2011). We bin the photometry in 30 s (gray filled circles) and 5-minute (black filled circles) intervals, and we overplot the best-fit instrumental models binned in 5-minute intervals for comparison (solid lines).

method applied to longer phase curve observations, see Wong et al. 2015). We utilize the raw flux values in a 3×3 grid of pixels centered on the position of the star and then normalize these individual pixel values by dividing by the total flux in each 3×3 postage stamp. We then incorporate these light curves into an instrumental model given by

$$F_{\text{model}}(t) = \frac{\sum_i w_i F_i(t)}{\sum_i F_i(t)}, \quad (1)$$

where F_{model} is the predicted stellar flux in an individual image, F_i is the measured flux in the i th individual pixel, and w_i is the weight associated with that pixel. We leave these weights as

⁸ Please see the IRAC High Precision Photometry Web site for details (<http://irachpp.spitzer.caltech.edu/page/Obs%20Planning>).

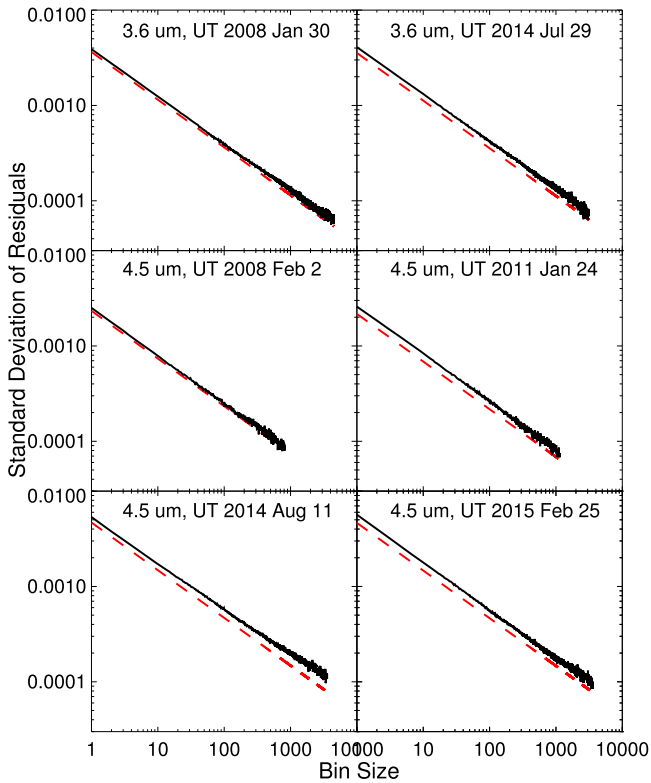


Figure 2. Standard deviation of the best-fit residuals as a function of the number of data points per bin (black lines). We overplot the expected $1/\sqrt{n}$ scaling for Gaussian noise as red dashed lines, where we have normalized these lines to match the standard deviation of the unbinned residuals.

free parameters in our fit and solve for the values that best match our observed light curves simultaneously with our eclipse fits.

Following the example of Deming et al. (2015), we fit this model to binned light curves with trial bin sizes ranging between 1 and 512 points sampled in steps of 2^n . In order to select the optimal aperture and bin size, we take our best-fit model coefficients for each binned light curve and calculate the corresponding model light curve for the unbinned data. We then subtract this model from the unbinned light curve in order to generate a vector of unbinned residuals, which we use to evaluate the noise properties of the data. As discussed in Deming et al. (2015) and Kammer et al. (2015), we create a metric to measure the noise properties of a given version of the photometry by calculating the rms variance of the residuals as a function of bin size (Figure 2). We then take the difference between a Gaussian noise model with $1/\sqrt{n}$ scaling and the observed rms as a function of bin size, square the difference, and sum over all bins. We then pick the version of the photometry that has the lowest amount of red noise as measured by our least-squares metric after discarding solutions where the rms of the best-fit residuals is more than 1.1 times higher than the lowest rms version of the photometry.

After determining the optimal aperture and bin size, we next consider versions of the photometry in which we trim varying amounts of data from the start of each light curve in order to remove the exponential ramp, which is another well-known feature of the IRAC 3.6 and 4.5 μm arrays (e.g., Lewis et al. 2013; Zellem et al. 2014). We examine the normalized light curves after detector effects have been removed and vary the trim duration until we identify the value that minimizes the red

noise in the best-fit residuals, in agreement with our criteria for selecting the optimal aperture and bin size. Because we do not include an exponential function as part of our model fit, this criterion serves to identify trim durations that minimize the presence of the exponential ramp in our data. We then rerun our previous analysis in order to ensure that our aperture and bin sizes are still optimal given this new trim duration.

We also considered an alternative approach in which we utilize a single metric of merit that balances our desire for reduced red noise with the increased white-noise penalty incurred in some realizations of the photometry. In this version of the analysis we calculate the least-squares difference between the rms as a function of bin size and the theoretical prediction for white (e.g., Gaussian and uncorrelated) noise using the predicted photon noise rather than the measured standard deviations of the residuals for the $n = 1$ bin. In this standard approach, the resulting least-squares difference therefore only captures the red-noise behavior of each light curve. With the new alternative approach, light curves with low red noise but a higher rms in the unbinned residuals would incur a modest penalty at the smallest bin sizes, where their rms would deviate more strongly from the predicted photon noise limit. We tried this metric for the two 3.6 μm observations and found that our top two to three apertures were the same as with the old metric, although the relative order of preference among these top three apertures was typically reshuffled. Our measured eclipse depths using the new best aperture choices were within 1.5σ and 0.5σ of the previous values for the 2008 and 2014 visits, respectively, and our corresponding average 3.6 μm eclipse depth changed by 0.5σ , to 168 ± 23 ppm. We find that, at least in this case, the choice of metric does not significantly affect our conclusions regarding the properties of GJ 436b’s atmosphere.

2.2. Eclipse Model and Uncertainty Estimates

We generate our secondary eclipse light curves using the routines from Mandel & Agol (2002), where we fix the planet–star radius ratio, orbital inclination, eccentricity e , longitude of periape ω , and ratio of the orbital semimajor axis to the stellar radius to their best-fit values from Lanotte et al. (2014). We allow individual eclipse depths and center-of eclipse times to vary as free parameters in our fits to the 3.6 μm data. We find that the eclipse depth in individual 4.5 μm observations is consistent with zero, and therefore we place a Gaussian prior on the phase of the secondary eclipse in order to constrain the best-fit eclipse time. We implement this prior as a penalty in χ^2 proportional to the deviation from the error-weighted mean center-of-eclipse phase and corresponding uncertainty from Knutson et al. (2011). Although we also calculate the best-fit eclipse orbital phase using the e and ω values from Lanotte et al. (2014) and find that it is consistent with the value from Knutson et al. (2011), the corresponding uncertainty is substantially larger than that reported in Knutson et al. (2011). This is not surprising, as the measured times of secondary eclipse constrain $e \cos \omega$, while $e \sin \omega$ is typically derived from fits to radial velocity data and has larger uncertainties (e.g., Pál et al. 2010; Knutson et al. 2014b). The uncertainties in the values for e and ω reported in Lanotte et al. (2014) are therefore likely to be dominated by the $e \sin \omega$, while $e \cos \omega$ is well measured from secondary eclipse photometry alone.

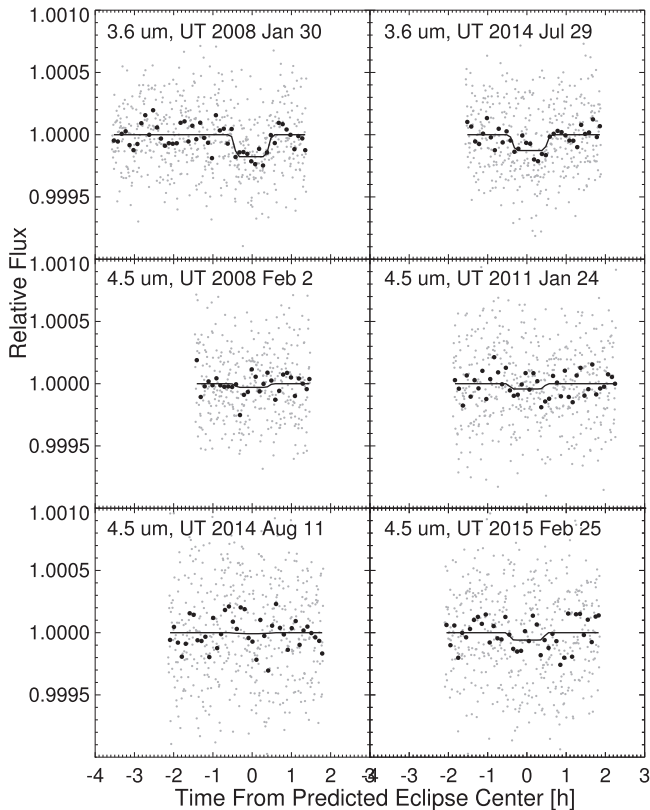


Figure 3. Normalized *Spitzer* 3.6 and 4.5 μm light curves as a function of time from the predicted center of eclipse, where we have divided out the best-fit instrumental model shown in Figure 1. The normalized flux is binned in 30 s (gray filled circles) and 5-minute (black filled circles) intervals, and best-fit eclipse model light curves are overplotted for comparison (solid lines).

We chose not to include a prior for our 3.6 μm fits because we wanted to derive an independent estimate of the eclipse center time and phase. However, to test the effect of this choice, we repeat our 3.6 μm fits including this prior on the eclipse phase and find that the uncertainties on the measured eclipse depths change by less than 0.1σ , as expected for cases where the eclipse is detected at a statistically significant level.

We fit our combined eclipse and instrumental noise model to each light curve using a Levenberg–Marquardt minimization routine with uniform priors on all parameters except the 4.5 μm eclipse time as described in the previous paragraph. Our model includes nine pixel weight parameters, two eclipse parameters, and a linear function of time in order to account for long-term instrumental and stellar trends. We show the resulting light curves and best-fit eclipse models after dividing out the best-fit instrumental noise model and linear function of time in Figure 3. Uncertainties on model parameters are calculated using a Markov chain Monte Carlo (MCMC) analysis with 10^6 steps initialized at the location of the best-fit solution from our Levenberg–Marquardt minimization. We trim any remaining burn-in at the start of the chain by checking to see where the χ^2 value of the chain first drops below the median value over the entire chain, and we trim all points prior to this step. We find that in all cases our probability distributions for the best-fit eclipse depths and times are Gaussian and do not show any correlations with other model parameters. We therefore take the symmetric 68% interval around the median parameter value as our 1σ uncertainties.

3. ATMOSPHERIC MODELING

We use a combination of self-consistent modeling and retrieval algorithms to model the atmosphere of GJ 436b and match its spectrum. The self-consistent modeling mirrors that used in Morley et al. (2015); our suite of tools includes a 1D radiative–convective model to calculate the P–T structure, a photochemical model to calculate the formation of hydrocarbons that may form hazes, and a cloud model to calculate cloud mixing ratios, altitudes, and particle sizes. We calculate spectra in different geometries and wavelengths using a transmission spectrum model, a thermal emission spectrum model, and an albedo model. We also use a retrieval model, CHIMERA (Line et al. 2012, 2013, 2014), to explore the thermal emission spectrum. In the following subsections we will briefly discuss each of these calculations.

We fit our models to the thermal emission and transmission spectra separately and then analyze the regions of parameter space where the same model parameters fit both the thermal emission and transmission spectra.

3.1. 1D Radiative–Convective Model

We calculate the temperature structures of GJ 436b’s atmosphere assuming radiative–convective equilibrium. These models are more extensively described in McKay et al. (1989), Marley et al. (1996, 1999, 2002), Burrows et al. (1997), Fortney et al. (2005, 2008), and Saumon & Marley (2008). Our opacity database for gases is described in Freedman et al. (2008, 2014). We calculate the effect of cloud opacity using Mie theory, assuming spherical particles. Optical properties of sulfide and salt clouds and soot haze are from a variety of sources and presented in Morley et al. (2012, 2013).

To calculate P–T profiles for models with greater than $50\times$ solar metallicity, we make the same approximation as used in Morley et al. (2015). We multiply the total molecular gas opacity by a constant factor (e.g., we multiply the $50\times$ solar opacities by 6 to approximate the opacity in a $300\times$ solar composition atmosphere). We change the abundances of hydrogen and helium separately to calculate collision-induced absorption. This approximation is appropriate for the results explored here; for future work, e.g., comparing models to *JWST* data, new k -coefficients at 100–1000 solar metallicity should be used.

3.2. Equilibrium Chemistry

After calculating the P–T profiles of models with greater than $50\times$ solar metallicity, we calculate the gas abundances assuming chemical equilibrium along that profile. We use the Chemical Equilibrium with Applications model (CEA; Gordon et al. 1984) to compute the thermochemical equilibrium molecular mixing ratios (for applications to exoplanets see Line et al. 2010, 2011; Visscher et al. 2010; Moses et al. 2011; Line & Yung 2013). CEA minimizes the Gibbs free energy with an elemental mass balance constraint given a local temperature, pressure, and elemental abundances. We include molecules containing H, C, O, N, S, P, He, Fe, Ti, V, Na, and K. We account for the depletion of oxygen due to enstatite condensation by removing 3.28 oxygen atoms per Si atom (Burrows & Sharp 1999). When adjusting the metallicity, all elemental abundances are rescaled equally relative to H, ensuring that the elemental abundances sum to 1.

Table 2
Uniform Prior Ranges on the Retrieved Parameters

Parameter	Range
$\log(\kappa_{\text{IR}})$ ($\text{cm}^2 \text{g}^{-1}$)	-3 to 0
$\log(\gamma_1, \gamma_2)$	-3 to 2
α	0-1
β	0-2
T_{int} (K)	100-400
M/H	10^{-4} to $10^4 \times$ solar
$\log(\text{C/O})^{\text{a}}$	-2 to 2
$\log(P_{\text{quench}})$ (bars)	-6 to 1.5

Note.

^a Solar $\log(\text{C/O})$ is -0.26.

3.3. Photochemical Haze Model

We use results from photochemical modeling in Line et al. (2011). Briefly, the computations use the Caltech/JPL photochemical and kinetics model, KINETICS (a fully implicit, finite difference code), which solves the coupled continuity equations for each species and includes transport via both molecular and eddy diffusion (Allen et al. 1981; Yung et al. 1984; Moses et al. 2005). We use results for $50 \times$ solar composition, $K_{zz} = 10^8 \text{ cm}^2 \text{ s}^{-1}$ (Figures 5–7 in Line et al. 2011).

We follow the approach developed in Morley et al. (2013) and used for GJ 1214b in Morley et al. (2015) to calculate the locations of soot particles based on the photochemistry. We sum the number densities of the five soot precursors (C_2H_2 , C_2H_4 , C_2H_6 , C_4H_2 , and HCN) to find the total mass in soot precursors. We assume that the soots form at the same altitudes as the soot precursors exist: we multiply the precursors’ masses by our parameter f_{haze} (the mass fraction of precursors that form soots) to find the total mass of the haze particles in a given layer. We vary both f_{haze} and the mode particle size as free parameters and calculate the optical properties of the haze using Mie theory.

3.4. Sulfide/Salt Cloud Model

To model sulfide and salt clouds, we use a modified version of the Ackerman & Marley (2001) cloud model (Morley et al. 2012, 2013, 2015). Cloud material in excess of the saturation vapor pressure of the limiting gas is assumed to condense into spherical, homogeneous cloud particles. We extrapolate the saturation vapor pressure equations from Morley et al. (2012) to high metallicities, which introduces some uncertainties but serves as a reasonable first-order approximation for the formation of these cloud species. Cloud particle sizes and vertical distributions are calculated by balancing transport by advection with particle settling.

3.5. Thermal Emission Spectra

We use a radiative transfer model developed in Morley et al. (2015) to calculate the thermal emission of a planet with arbitrary composition and clouds. Briefly, this model includes the C version of the open-source radiative transfer code `disort` (Stamnes et al. 1988; Buras et al. 2011), which uses the discrete-ordinate method to calculate intensities and fluxes in multiple-scattering and emitting layered media.

3.6. Albedo Spectra

We calculate albedo spectra following the methods described in Toon et al. (1977, 1989), McKay et al. (1989), Marley et al. (1999), Marley & McKay (1999), and Cahoy et al. (2010). Here, we use the term “geometric albedo” to refer to the albedo spectrum at full phase ($\alpha = 0$, where the phase angle α is the angle between the incident ray from the star to the planet and the line of sight to the observer):

$$A_g(\lambda) = \frac{F_p(\lambda, \alpha = 0)}{F_{\odot,L}(\lambda)}, \quad (2)$$

where λ is the wavelength, $F_p(\lambda, \alpha = 0)$ is the reflected flux at full phase, and $F_{\odot,L}(\lambda)$ is the flux from a perfect Lambert disk of the same radius under the same incident flux.

3.7. Retrieval Model

To more thoroughly explore the chemically plausible parameter space allowed by the emission spectrum, we employ the chemically consistent atmospheric retrieval scheme described in Kreidberg et al. (2015) and Greene et al. (2016) based on the CHIMERA (Line et al. 2013, 2014) emission forward model. The retrieval uses the six-parameter analytic radiative equilibrium temperature profile scheme of Parmentier & Guillot (2014) (for implementation within the emission retrieval see Line et al. 2013), where the free parameters are the infrared opacity (κ_{IR}), the ratio of the visible to infrared opacity for two visible streams (γ_1, γ_2), the partitioning between the two visible streams (α), scaling to the top-of-atmosphere irradiation temperature (β , to accommodate for the unknown albedo and redistribution), and finally the internal temperature (T_{int}). These parameters are all free parameters, not recalculated to be consistent with the derived abundances (Line et al. 2012).

The molecular abundances are initially computed along the temperature profile under the assumption of thermochemical equilibrium (using the Chemical Equilibrium with Applications routine; Gordon & McBride 1994, 1996; Line et al. 2010, 2011; Moses et al. 2011) given the bulk atmospheric metallicity ([M/H]) and carbon-to-oxygen ratio (C/O). To account for possible disequilibrium chemistry, we include a “quench pressure” parameter (P_{quench}) whereby the abundances of H_2O , CH_4 , and CO above the quench are fixed at their quench pressure values, a valid representation of many disequilibrium models (e.g., Line et al. 2011; Moses et al. 2011; Zahnle & Marley 2014). The temperature profile and chemistry parameters result in a total of nine free parameters. Bayesian estimation is performed using a multimodal nested sampling algorithm (Feroz et al. 2009) implemented with the PYMULTINEST routine (Buchner et al. 2014) recently employed in Line & Parmentier (2016), with generous uniform priors on each parameter (see Table 2).

4. RESULTS

4.1. Observations

The new eclipse depths are shown in Table 3 and Figure 4. Our eclipse depths of 155 ± 22 ppm at $3.6 \mu\text{m}$ and 34_{-16}^{+20} ppm at $4.5 \mu\text{m}$ are consistent to 1σ with those published in Lanotte et al. (2014) (177 ± 45 and 28_{-18}^{+25} ppm, respectively), with a moderate reduction in the uncertainties in both bands. This result serves as confirmation of the high flux at $3.6 \mu\text{m}$ compared to $4.5 \mu\text{m}$.

Table 3
Best-fit Eclipse Parameters

λ (μm)	UT Start Date	F_p/F_* (ppm)	$F_p/F_{*,\text{avg}}$ (ppm) ^a	T_{bright} (K) ^a	T_s ^b	$O - C$ (days) ^c
3.6	2008 Jan 30	176 ± 30	155 ± 22	876_{-28}^{+26}	4496.4888 ± 0.0012	-0.0007 ± 0.0012
3.6	2014 Jul 29	127 ± 34	6868.0691 ± 0.0046	-0.0030 ± 0.0046
4.5	2008 Feb 02	29 ± 36	34 ± 20	$<634^e$	4499.1334^d	...
4.5	2011 Jan 24	43 ± 36	5585.7756^d	...
4.5	2014 Aug 11	59 ± 44	6881.2856^d	...
4.5	2015 Feb 25	7 ± 43	7079.5779^d	...

Notes.

^a We report the error-weighted mean eclipse depths at 3.6 and 4.5 μm . Brightness temperatures are calculated using a PHOENIX stellar model interpolated to match the published stellar temperature and surface gravity from von Braun et al. (2012).

^b $\text{BJD}_{\text{UTC}} - 2,450,000$.

^c Observed minus calculated eclipse times, where we have accounted for the uncertainties in both the measured and predicted eclipse times, as well as the light-travel time delay in the system. We calculate the predicted eclipse time using the best-fit eclipse orbital phase from Knutson et al. (2011).

^d We allow the eclipse times in this bandpass to vary as free parameters in our fit, but we use the orbital phase and corresponding uncertainty from Knutson et al. (2011) as a prior constraint in the fit.

^e 2σ upper limit based on the error-weighted average of the four 4.5 μm eclipse measurements.

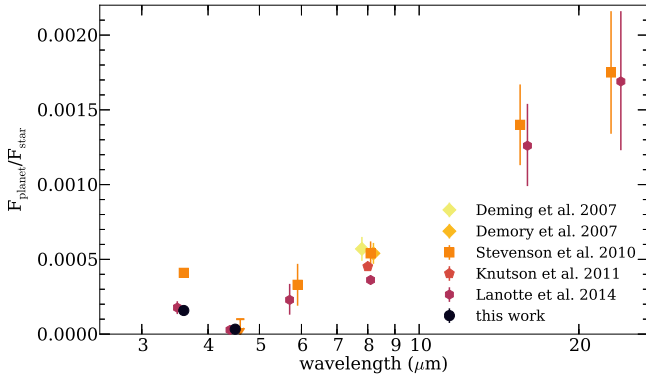


Figure 4. Eclipse depths in the six *Spitzer* bandpasses from the literature and this work. Different publications are offset slightly in wavelength for clarity; darker colors indicate later years.

4.2. Self-consistent Modeling

We ran a variety of models from 50–1000 \times solar metallicity, varied heat redistribution (planet-wide average and dayside average), internal temperatures (T_{int}) from 100 to 400 K, with clouds ($f_{\text{sed}} = 0.01$ –1), and hazes with particle sizes from 0.01 to 1 μm and f_{haze} from 1% to 30%. We compare each model to the thermal emission photometry from this work (3.6 and 4.5 μm) and from Lanotte et al. (2014) (5.6, 8.0, 16 μm), using a chi-squared analysis to assess relative goodness of fit between the models.

We show example P–T profiles along with cloud condensation curves in Figure 5. Raising the internal temperature, T_{int} , increases the temperature of the deep atmosphere ($P \gtrsim 0.1$ bars). The heat redistribution of incident stellar flux controls the temperature in the upper atmosphere. GJ 436b’s profile crosses condensation curves of sulfides and salts, suggesting that if the atmosphere is cloudy, those clouds may be composed of Na_2S , KCl, and ZnS.

4.2.1. Best-fit Fiducial Model

Of the 288 models in our grid of cloudy and cloud-free planets, our nominal best-fit set of parameters is as follows:

1. 200 \times solar metallicity;
2. $T_{\text{int}} = 240$ K;

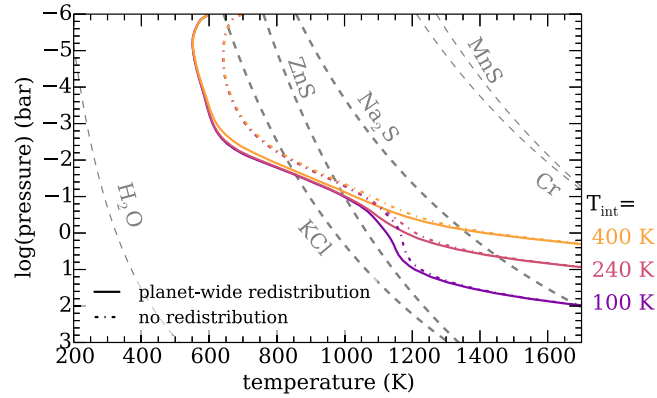


Figure 5. P–T profiles with condensation curves. All models are cloud-free with 300 \times solar composition. Solid lines show models with $T_{\text{int}} = 100, 240,$ and 400 K and planet-wide heat redistribution. Dot-dashed lines show models with the same T_{int} values but with no heat redistribution (dayside temperature). Condensation curves show where the vapor pressure of a gas is equal to the saturation vapor pressure; cloud material condenses where the P–T profile intersects a condensation curve.

3. $f_{\text{sed}} = 1$ sulfide/salt clouds;
4. disequilibrium chemistry via quenching;
5. full heat redistribution (planet-wide average P–T profile).

This model provides an excellent fit to the transmission spectrum ($\chi_{\text{red}}^2 < 1$ assuming 3 degrees of freedom), though an inadequate fit to the thermal emission ($\chi_{\text{red}}^2 \sim 13$ assuming 3 degrees of freedom). We show the thermal emission and transmission spectra in Figure 6.

4.2.2. Equilibrium and Disequilibrium Chemistry

As has been discussed in the literature (Stevenson et al. 2010; Line et al. 2011; Moses et al. 2013), GJ 436b’s high 3.6 μm flux and low 4.5 μm flux indicate that it likely has a high abundance of CO and CO_2 relative to CH_4 . Since equilibrium chemistry for an object at GJ 436b’s temperature would instead result in high abundances of CH_4 at metallicities similar to Neptune, this indicates that GJ 436b’s chemistry is in disequilibrium. This disequilibrium may be due to a combination of vertical mixing, photochemistry, and other effects (Line

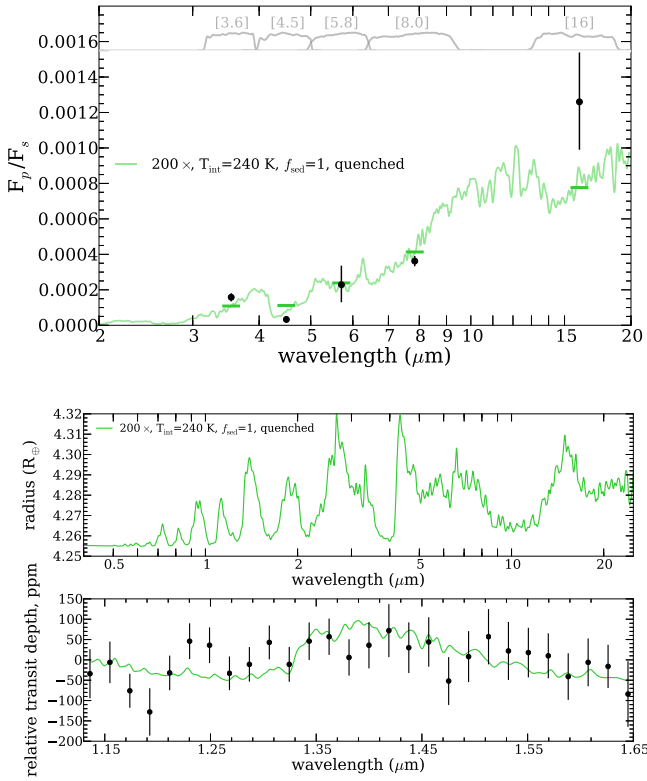


Figure 6. Best-fit thermal emission and transmission spectra. Top panel: thermal emission spectrum of the best-fit model from the suite of forward models compared to the data. The model is shown as a green line, with synthetic model photometry shown as horizontal lines at the central wavelength of the filter. Data are shown as black points with 1σ error bars. The filter functions for the photometry are shown as gray lines in the top panel. Bottom panels: transmission spectrum of the same best-fit thermal emission model from the suite of forward models compared to the data. The model is shown as a green line in both panels. The *HST*/WFC3 transmission spectrum is shown as black points with 1σ error bars in the bottom panel.

et al. 2011). Here, we approximate the effect of disequilibrium chemistry by “quenching” the abundances of the carbon species (CO , CO_2 , CH_4) in the atmosphere at deep pressures (10 bars), effectively setting the abundances of these species to be constant throughout the atmosphere.

The resulting effect of disequilibrium chemistry on spectra is shown in Figure 7. In equilibrium, the model predicts that GJ 436b would be very faint at $3.6 \mu\text{m}$ and progressively brighter at redder wavelengths. In disequilibrium, as is observed in the data, the planet is predicted to be brighter at $3.6 \mu\text{m}$, due to decreased absorption by CH_4 . In general, even the models that include disequilibrium chemistry overpredict the brightness at $4.5 \mu\text{m}$ compared to the observed flux, despite the higher abundance of CO and CO_2 in disequilibrium.

4.2.3. Metallicity

Increasing the metallicity of GJ 436b’s atmosphere allows us to fit both the thermal emission and transmission spectrum more accurately. There are two reasons for this. As has been discussed at length in Moses et al. (2013), high-metallicity atmospheres are predicted, in equilibrium or disequilibrium, to have higher abundances of CO and CO_2 relative to CH_4 . Pushing the chemistry to CO/CO_2 -rich compositions is crucial to match GJ 436b’s thermal emission. We show this effect in Figure 8; models at high metallicities have higher flux at 3.6

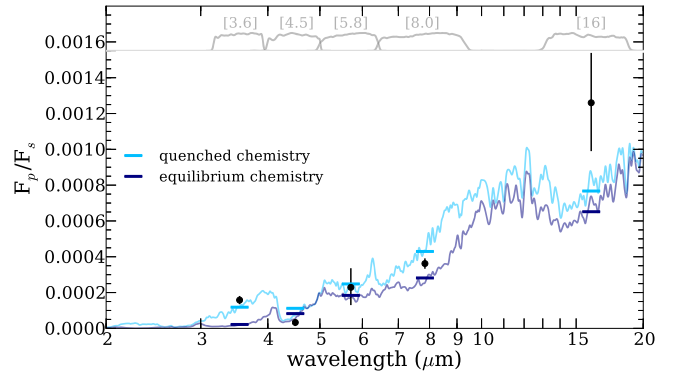


Figure 7. Effect of chemistry on thermal emission spectrum. Both models assume $300\times$ solar metallicity, $f_{\text{sed}} = 1$ sulfide/salt clouds, planet-wide heat redistribution, and $T_{\text{int}} = 240 \text{ K}$. The dark-blue line and horizontal bars show a model spectrum and photometry assuming equilibrium chemistry; the light-blue line and horizontal bars show the same model, but with the chemistry quenched at the 10 bar abundances throughout the atmosphere.

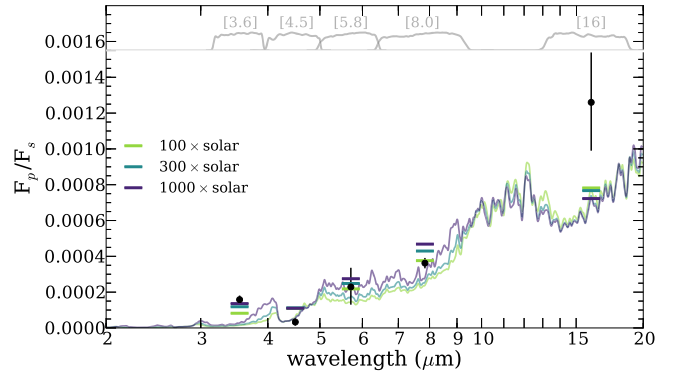


Figure 8. Effect of metallicity on thermal emission. Each model assumes equilibrium chemistry, $f_{\text{sed}} = 1$ sulfide/salt clouds, planet-wide heat redistribution, and $T_{\text{int}} = 240 \text{ K}$. Metallicities of 100, 300, and $1000\times$ solar metallicity are shown. Increasing the metallicity decreases the CH_4 abundance and increases CO and CO_2 abundance.

and $8 \mu\text{m}$, due to the change in chemistry. We find that this effect partially saturates at metallicities greater than $300\times$ solar.

High metallicities also make it much easier to flatten the transmission spectrum of GJ 436b sufficiently to match the featureless *HST*/WFC3 transmission spectrum even in the absence of clouds (Knutson et al. 2014a). In Figure 9 we show cloud-free models for different metallicities. While at metallicities lower than $1000\times$ solar metallicity clouds are required to sufficiently flatten the spectrum, for models above $1000\times$ solar metallicity even cloud-free models have high enough mean molecular weights that the sizes of the features, which scale according to the scale height of the atmosphere, are small enough that they appear featureless at the S/N of the data.

4.2.4. Tidal Heating

As a Neptune-sized planet orbiting an old star, without an additional energy source, GJ 436b’s interior temperature T_{int} would be $\sim 60 \text{ K}$, slightly warmer than Neptune, which has a $T_{\text{int}} \sim 50 \text{ K}$ (Fortney et al. 2007). However, GJ 436b is on an eccentric orbit ($e \sim 0.15$) despite orbiting its star at a semimajor axis where it is predicted to have a tidally circularized orbit, indicating that its interior may still be heated by tidal dissipation. Moses et al. (2013) and Agúndez et al.

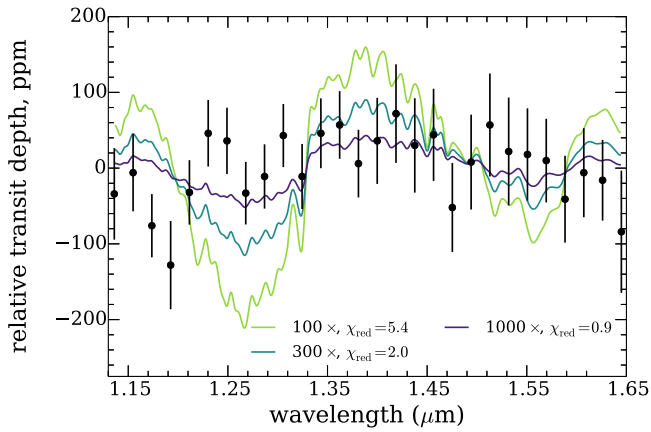


Figure 9. Effect of metallicity on transmission spectrum. Each model is cloud-free, with planet-wide heat redistribution, equilibrium chemistry, and $T_{\text{int}} = 240$ K. Metallicities of 100, 200, 300, and 1000 \times solar metallicity are shown. Increasing the metallicity decreases the CH_4 abundance and increases CO and CO_2 abundance.

(2014) both considered the effect of tidal heating, noting that a hotter interior changes the chemistry of the deep interior and therefore the resulting emission spectrum.

Increasing T_{int} tends to move the deep P–T profile (see Figure 5) to regions with high CO/ CO_2 and lower CH_4 abundances (see Figure 10), which allows us to better match the observed spectrum. Heating the deep atmosphere also increases the effective temperature of the atmosphere by changing the P–T profile, increasing flux at all *Spitzer* wavelengths. This effect is shown in Figure 11 for three different T_{int} values (100, 240, and 400 K). Best-fit models cluster around $T_{\text{int}} = 240$ K, a temperature that allows us to match the 3.6, 5.6, and 8.0 μm points relatively well, while overpredicting the 4.5 μm flux somewhat.

We note that this is the first indication that the internal temperature of a planet has an important and observable effect on the emission spectrum of a transiting planet.

4.2.5. Clouds

Clouds increase opacity across all wavelengths as (relatively) gray absorbers. This means that including clouds decreases flux between absorption features (e.g., at 3.6 and 8.0 μm for GJ 436b’s composition) and somewhat less significantly at the locations of absorption features, where the planet is already dark. Thinner clouds ($f_{\text{sed}} = 0.3$ –1 in our parameterization) alter the spectrum slightly, while thicker clouds ($f_{\text{sed}} \leq 0.1$) create a blackbody-like spectrum with the temperature of the top of the cloud. As shown in Figure 12, when cloudy models are compared with the observed photometry of GJ 436b, these thick clouds significantly underpredict the flux at 3.6 μm especially.

In transmission, clouds flatten the spectrum without increasing the mean molecular weight of molecular gas in the atmosphere. As discussed above, for metallicities $\sim 1000\times$ solar, no additional cloud opacity is needed to match the featureless spectrum ($\chi_{\text{red}}^2 \sim 1$ for all models). At 300 \times solar metallicity, thin clouds ($f_{\text{sed}} = 1$) adequately obscure the spectral features, whereas for a Neptune-like 100 \times solar composition, $f_{\text{sed}} = 0.3$ clouds are required. In the Ackerman & Marley (2001) prescription, lower f_{sed} values indicate less

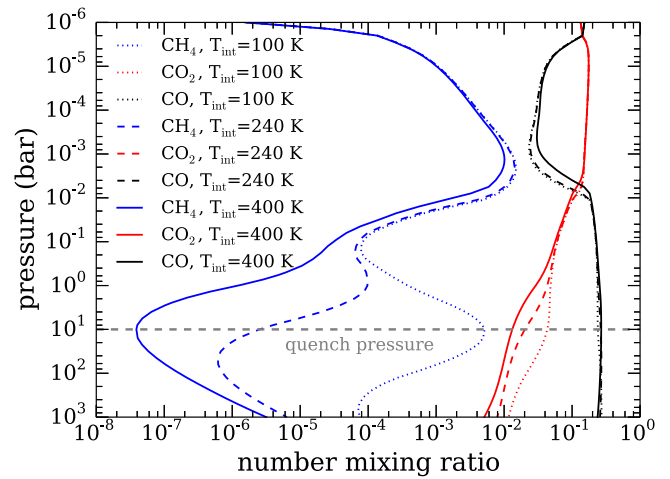


Figure 10. Abundances of major carbon-bearing species in chemical equilibrium. All models have a composition of 1000 \times solar metallicity and a planet-wide average P–T profile. Different T_{int} values are shown with different line styles, and each molecule (CH_4 , CO, CO_2) is shown in a different color. The fiducial quench pressure used in the self-consistent modeling is shown as a horizontal dashed line. Note that increasing the internal temperature decreases the CH_4 abundance in the deep atmosphere.

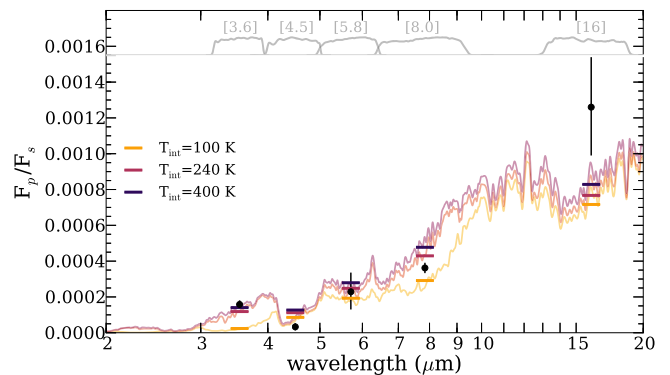


Figure 11. Effect of tidal heating on thermal emission. Each model assumes 300 \times solar metallicity, quenched chemistry, $f_{\text{sed}} = 1$ sulfide/salt clouds, and planet-wide heat redistribution. The tidally heated atmospheres (240 and 400 K) have higher abundances of CO and CO_2 and lower abundances of CH_4 , due to the hotter deep atmosphere (where the chemistry is quenched). Tidal heating also increases the T_{eff} of the planet by changing the temperature profile, increasing the emergent flux at all wavelengths.

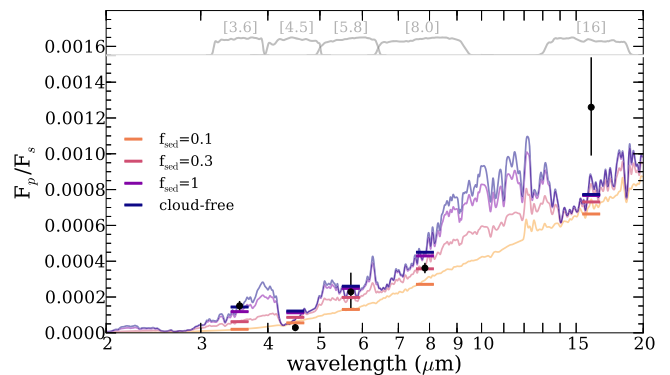


Figure 12. Effect of sulfide/salt clouds on thermal emission. Each model uses the same P–T profile and assumes 300 \times solar metallicity, quenched chemistry, planet-wide heat redistribution, and $T_{\text{int}} = 240$ K. A cloud-free model and cloudy models with $f_{\text{sed}} = 0.03$ –1 are shown. Cloud opacity decreases the thermal emission across the spectrum. Models with moderate clouds ($f_{\text{sed}} = 0.3$ –1) fit the *Spitzer* points best.

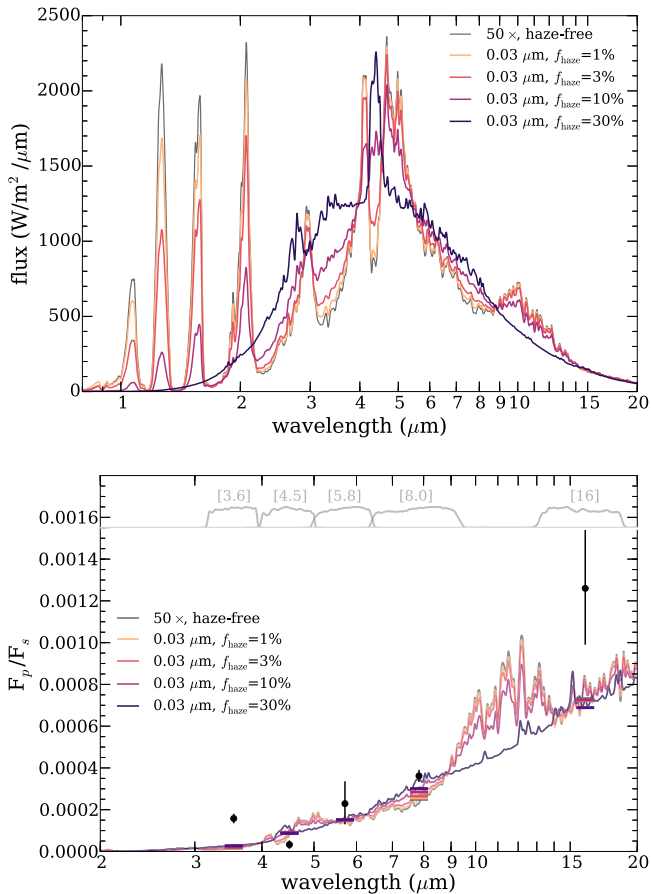


Figure 13. Effect of photochemical hazes on thermal emission. The top panel shows the emergent flux from the planet. All models have $50\times$ solar metallicity, equilibrium chemistry, and planet-wide heat redistribution. The gray line shows a cloud-free model, and the colored lines show a progression of hazy models with hazy-forming efficiency parameter f_{haze} varying from 1% to 30%. The bottom panel shows the same models, but dividing by the flux of the host star to compare to the measured photometry.

efficient sedimentation, causing smaller particle sizes and more lofted clouds.

4.2.6. Photochemical Hazes in GJ 436b

We investigate the effect of photochemical hazes on the thermal emission spectrum of GJ 436b. Morley et al. (2015) showed that it is possible for optically thick photochemical hazes (such as those postulated to exist in GJ 1214b) to cause a temperature inversion in the upper atmospheres of planets. This can change the spectrum such that molecules that would normally be seen in absorption in a planet without a temperature inversion such as methane are actually seen in emission in an atmosphere with a temperature inversion. We tested whether this process could be happening on GJ 436b and causing the observed thermal emission.

The results of this investigation are summarized in Figure 13. The top panel shows the thermal emission of the planet alone. We find that it is possible to create a temperature inversion with dark soot-like photochemical haze in GJ 436b, especially for relatively small particle sizes. As expected, methane is seen in emission, significantly brightening the model spectrum at $3.6\ \mu\text{m}$ compared to a haze-free model. As in Morley et al. (2015), CO_2 at $4.3\ \mu\text{m}$ is also predicted to be seen in emission at Neptune-like metallicities (in this case $50\times$ solar metallicity). In the bottom

panel, we show the planet–star flux ratio; here it becomes clear that the hazy model does not fit the observations significantly better than the haze-free model. In particular, the model spectrum is much fainter than the planet’s $3.6\ \mu\text{m}$ photometric point. The $4.5\ \mu\text{m}$ flux, despite the significant changes to the shape of the spectrum across the bandpass, remains nearly identical across the range of hazy models tested.

In general, we find that even though a temperature inversion in a methane-rich atmosphere can increase the $3.6\ \mu\text{m}$ flux, it is not a significant enough effect to match the observed flux, and furthermore, the flux within the $4.5\ \mu\text{m}$ region can also increase owing to emission in the CO_2 bandpass. We conclude that photochemical hazes cannot erase the need for an atmosphere with significant CO and CO_2 and a low abundance of CH_4 . This required low- CH_4 atmospheric composition, in turn, reduces the likelihood that carbon-based photochemical hazes will be significant in the atmosphere (Fortney et al. 2013).

4.3. Retrievals

We have shown in Section 4.2 that we favor models at high metallicity, with both disequilibrium chemistry and tidal heating; these three properties combine to maximize the CO/ CO_2 abundances and minimize CH_4 abundance, allowing the models to match approximately with the measured photometry. Retrieval models provide a quantitative way to test these conclusions and fully explore parameter space beyond our self-consistent model grids.

We find that retrieval methods draw similar conclusions to the self-consistent modeling; GJ 436b appears to be very high metallicity, with evidence for both deeply quenched disequilibrium chemistry and thermal heating of the deep interior. For the dayside thermal emission spectrum, the best-fit retrieved solution has a goodness of fit divided by number of data points $\chi^2/N = 2.0$, compared to $\chi^2/N = 5.2$ for the best self-consistent thermal emission spectrum, indicating a significantly improved fit. A comparison of the Bayesian information criteria (BIC) reveals that additional parameters used in the retrieval fitting are necessary, with a BIC of ~ 26 for the best-fit retrieved solution and ~ 34 for the best-fit self-consistent solution.

4.3.1. Retrieved Posterior Probability Distributions

Retrieved posterior probability distributions and correlations are shown in the stair-pair plot in Figure 14 for five of the nine free parameters in the retrieval: β , T_{int} , $[\text{M}/\text{H}]$, $\log(\text{C}/\text{O})$, $\log(P_{\text{quench}})$. The best-fit models have the following:

1. High metallicity. The maximum likelihood model has a metallicity of $\sim 6000\times$ solar metallicity, with a 3σ lower limit on the metallicity of $106\times$ solar.
2. Disequilibrium chemistry. The maximum likelihood model has a quench pressure around 9 bars (with a wide range of values for P_{quench} allowed).
3. Enhanced internal temperature. The maximum likelihood T_{int} is 336 K (with large uncertainties), indicating that tidal heating may be increasing GJ 436b’s internal temperature, in agreement with the tidally heated self-consistent models.
4. Solar C/O ratio. The maximum likelihood C/O ratio is 0.70, with a sharp cutoff at higher C/O ratios and a long tail to lower C/O ratios.

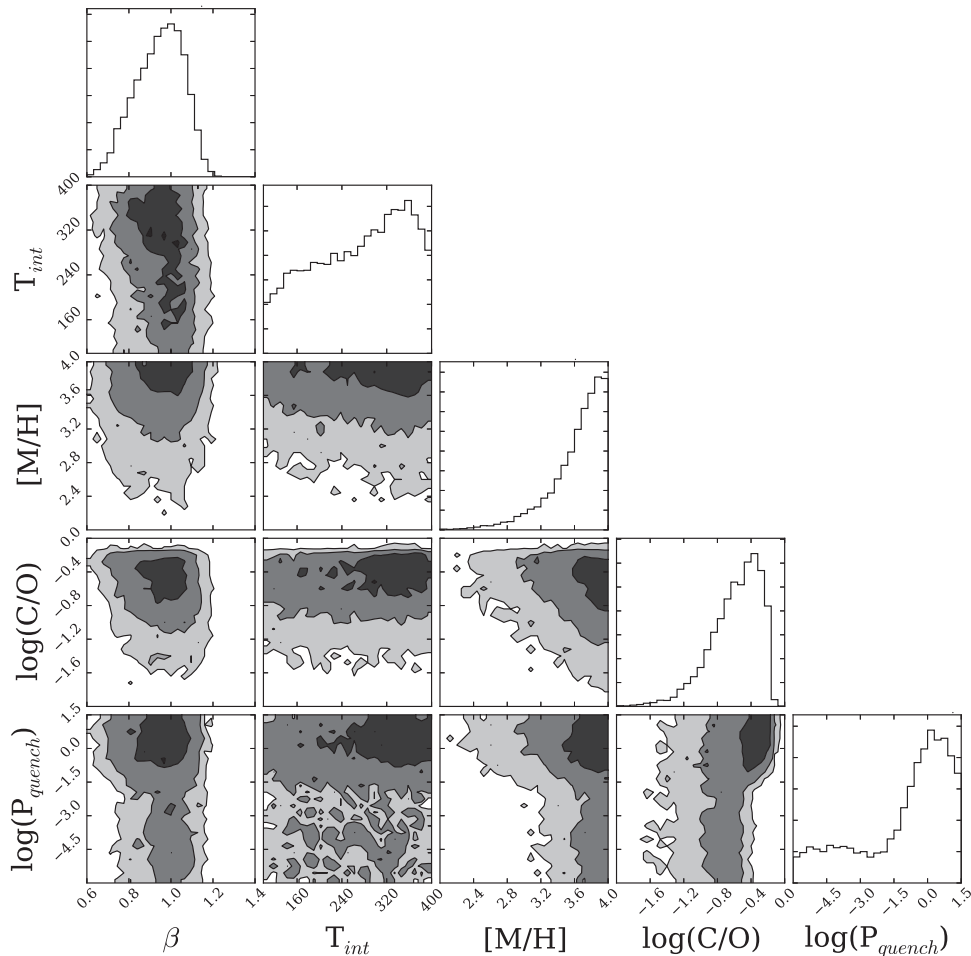


Figure 14. Posterior probability distributions and correlations. The top panel (histogram) shows the posterior probability distribution for each parameter, marginalized over all other parameters. The other panels show 2D contour plots that represent the correlations between each pair of parameters, where the regions from darkest to lightest represent the 1σ , 2σ , and 3σ contours.

In Figure 15 we compare the retrieved P–T profile to self-consistent models at $300\times$ solar metallicity. We find that the retrieved profile is in remarkable agreement with self-consistent models that include the effect of tidal heating in the deep interior. Our best-fit T_{int} from the self-consistent modeling approach (240 K) falls within the 2σ range of the retrieved profile.

The contribution functions for each of the *Spitzer* bandpasses are also shown in Figure 15. The $3.6\ \mu\text{m}$ band probes the deepest pressures, probing pressures as high as 1 bar. As expected, comparing the contribution functions to the range of P–T profiles found by the retrieval, the spread in allowed P–T profiles increases for pressures deeper than 1 bar. The other wavelengths probe lower pressures of the atmosphere, with 5.8 and $8.0\ \mu\text{m}$ centered around 0.05 bars and $16\ \mu\text{m}$ centered around 0.003 bars. The $4.5\ \mu\text{m}$ bandpass has the largest range of pressures, with a peak at deep pressures (0.2 bars) and a long tail to low pressures, unsurprising given that the band covers the spectrum where the modulation is the greatest.

Figure 16 shows the best-fit retrieved range of spectra compared to both the data and the best-fit self-consistent model. The retrieved best fit is statistically and by eye a somewhat better fit to the data than the self-consistent models. In particular, it has higher flux at $3.6\ \mu\text{m}$ and lower flux at

$4.5\ \mu\text{m}$. Both the retrieved and self-consistent models fit the 5.6 and $8.0\ \mu\text{m}$ points well; the $16\ \mu\text{m}$ photometry is underestimated by both models, though the error bar is large.

5. DISCUSSION

5.1. Predictions for Reflected Light Spectra

Cloud properties have the strongest effect on the predicted reflected light spectrum of GJ 436b. Cloud-free models are dark from 0.6 to $1\ \mu\text{m}$ ($A_g < 1\%$) and somewhat brighter (up to $A_g \sim 10\%$) at bluer wavelengths, as is generally true for cloudless giant planets (Marley et al. 1999; Sudarsky et al. 2000). Thinner clouds ($f_{\text{sed}} = 0.3\text{--}1$) are brighter, with albedos between a few percent and tens of percent. Thicker clouds ($f_{\text{sed}} = 0.1$) have the brightest albedos from 0.6 to $1\ \mu\text{m}$, up to nearly 30%. Some example cloudy spectra are shown in the top panel of Figure 17.

Other properties have weaker effects on the reflected light spectrum for this planet. For example, models with metallicities from $100\times$ to $300\times$ solar metallicity are shown in the bottom panel of Figure 17. Increasing the metallicity (which also changes the cloud) increases the geometric albedo across the spectrum.

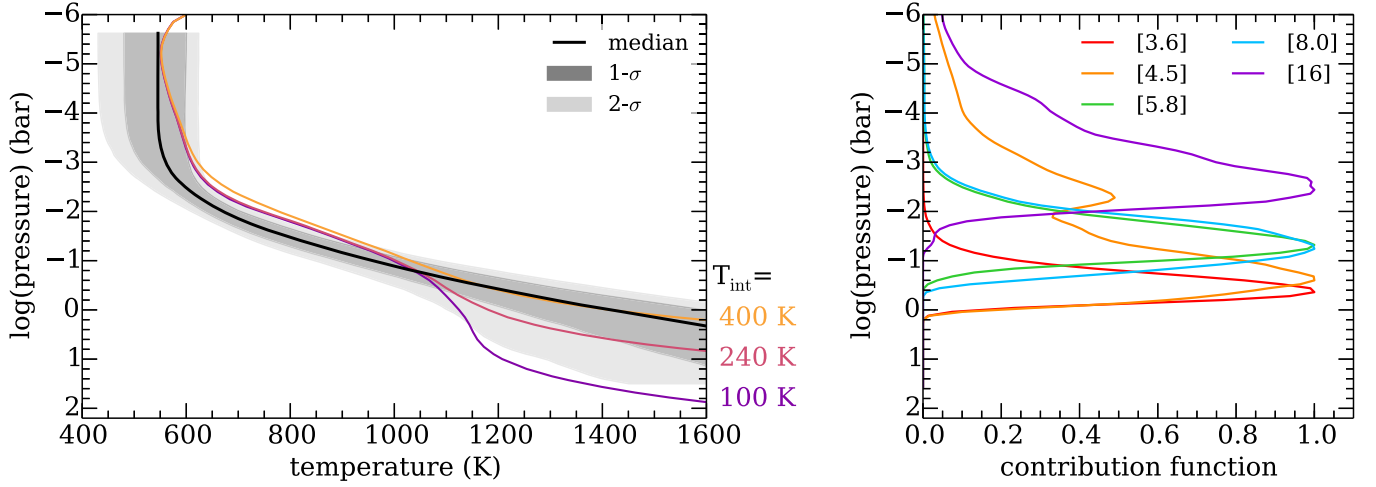


Figure 15. P–T profiles and contribution functions for each bandpass. The left panel shows P–T profiles of both retrieved and self-consistent models. The black line indicates the median retrieved profile, while the dark- and light-gray shaded regions represent the 1σ and 2σ confidence regions, respectively. The colored lines show self-consistent models with planet-wide heat redistribution and T_{int} of 100, 240, and 400 K. Note the good agreement between the tidally heated (240–400 K) models and the retrieved profile. The right panel shows contribution functions for each of the five bandpasses for a representative retrieval model. The shortest-wavelength 3.6 μm band probes the deepest wavelengths, while the 16 μm band probes the shallowest.

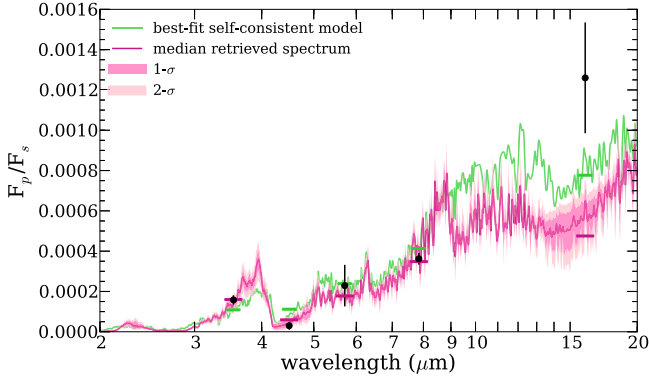


Figure 16. Retrieved model compared to data and best-fit self-consistent model. The pink line and shaded dark- and light-pink regions are the median fit, 1σ , and 2σ confidence intervals, respectively. The green line is the best-fit self-consistent model ($200\times$ solar metallicity, $T_{\text{int}} = 240$ K, $f_{\text{sed}} = 1$, quenched disequilibrium chemistry).

5.2. Speculations on Missing Physics

The fact that the reduced χ^2 of both the self-consistent and retrieval models are greater than ~ 1 (and assuming that the error bars on the data points are not underestimated at all of the wavelengths measured) suggests that there is physics not being accounted for in both modeling approaches. One obvious suggestion is that there is an additional absorbing molecule that is not included that absorbs in the mid-infrared, particularly in the [4.5] bandpass. The bright [3.6] point could be enhanced by an emission mechanism (e.g., Casewell et al. 2015) that operates in that bandpass (but not at [4.5]). Both of these “additional molecule” explanations are speculative and require further study. Some other potential differences between the models and reality include 2D/3D effects, if the surface is nonuniform in temperature, chemistry, or cloud properties as the models are calculated in 1D; however, 3D modeling in Lewis et al. (2010) shows virtually no temperature variation (see also Section 5.7). Clouds are not included in the retrievals, though there is no smoking-gun evidence for clouds in the self-consistent models where they are

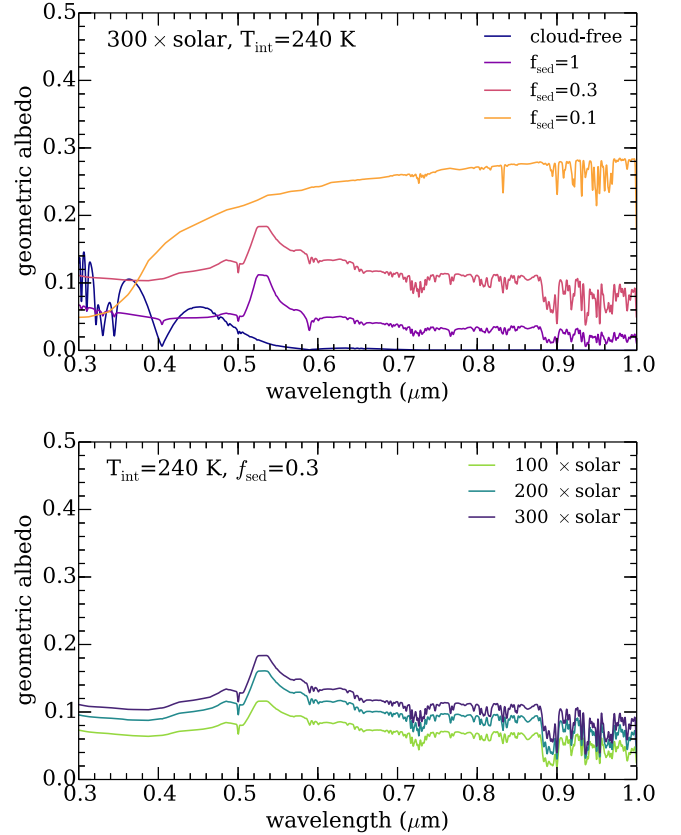


Figure 17. Predicted albedo spectra. Top panel: models with $300\times$ solar metallicity, $T_{\text{int}} = 240$ K. A cloud-free model and models with cloud parameter f_{sed} from 0.03 to 1 are shown. Bottom panel: models with $T_{\text{int}} = 240$ K and $f_{\text{sed}} = 0.3$. Metallicities from $100\times$ to $300\times$ solar are shown.

included. The choice of analytic P–T profile for the retrievals could also play a role in shaping the spectrum. Certainly the higher-resolution spectra that the *James Webb Space Telescope* (*JWST*) will provide will shed light on these speculations (see Section 5.4).

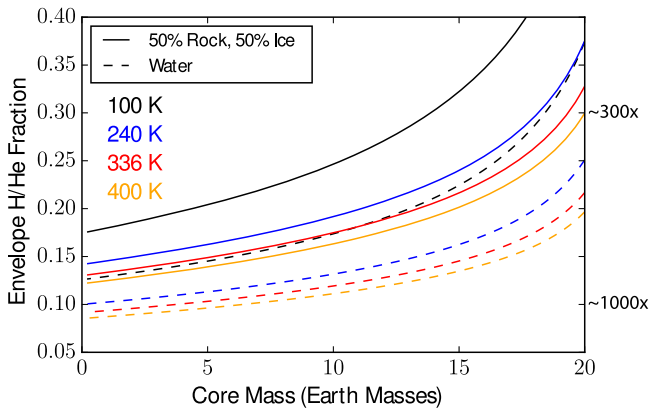


Figure 18. Core mass vs. envelope H/He fraction required to match GJ 436b’s measured mass and radius. Models that include a rock/ice core and mix of H/He and rock/ice in the envelope are shown as solid lines, while models that include a water ice core and mix of H/He and water in the envelope are shown as dashed lines. Different colors represent different interior temperature T_{int} . Approximate conversions between envelope H/He fraction and atmospheric metallicity for 1000 \times and 300 \times solar metallicity are shown at the right.

5.3. Are Very High Metallicities Reasonable?

We find that the best-fit atmospheric models have high metallicities, but it remains to be seen whether these values are physically realistic. GJ 436b has a different host star, equilibrium temperature, and orbit than the ice giants in our own solar system, so it likely formed and evolved in very different conditions. The maximum metal enrichment of the envelope of a Neptune-mass exoplanet is not yet known. Studies of this to date, including Fortney et al. (2013), have suggested that a diverse range of outcomes might be expected for planets in this intermediate-mass regime between Earth and Saturn, with potentially high atmospheric enrichments in some cases.

Furthermore, because of the uncertainty in the internal entropy of GJ 436b, its mass and radius do not provide strong limits on the metal enrichment of the envelope. Nettelmann et al. (2010) find that a minimum H/He fraction of $10^{-3} M_p$ is necessary to match the radius. This very low H/He fraction would require a warm planetary interior, as is favored by the best-fit thermal emission spectra in this work.

In Figure 18 we show the results from interior models (Thorngrén et al. 2016), which show the envelope H/He mass fraction required to match GJ 436b’s mass and radius measurements for core masses from 0 to $20 M_{\oplus}$. These one-dimensional interior models include an inert core composed of either 50% rock and 50% ice or 100% water ice. Each model has a homogeneous convective envelope made of an H/He-rock-ice or H/He-ice mixture. We use equations of state from Thompson (1990) (water and water-rock) and Saumon et al. (1995) (H/He) and atmospheric models from Fortney et al. (2007). Neither the pure water nor water-rock equations of state are dependent on temperature; since GJ 436b has a hot interior, we expect that the true equation of state of its interior will be more accurately matched by the water ice equation of state, even though the composition is likely a mix of heavy elements.

We find that for the best-fit T_{int} of 336 K the maximum envelope metallicity is somewhat lower than 1000 \times solar metallicity. For a $20 M_{\oplus}$ core, the minimum envelope metallicity required to match the observed mass and radius is $\sim 300\times$ solar metallicity (though the envelope could be less

enriched if the core is somewhat larger than $20 M_{\oplus}$. These calculations suggest that the very high metallicities above 1000 \times solar metallicity explored by our retrieval models are not physically realistic for this planet, but metallicities above 300 \times solar are favored.

Very high metallicities are only possible if accretion and subsequent enrichment are dominated by rocky rather than icy materials; Fortney et al. (2013) show that if the majority of accretion is from icy material, the hydrogen in those ices is also accreted and the maximum metal enrichment is $\sim 600\times$ solar metallicity. Though we cannot currently distinguish between compositions less than or greater than 600 \times solar composition, if GJ 436b is indeed very metal enhanced, it likely formed in a region with more refractory than volatile materials available.

5.4. Role of JWST Spectral Observations

JWST will amplify our understanding of warm Neptunes like GJ 436b by providing spectra instead of photometry, breaking some of the current degeneracies. For example, examining the spectra in Figure 16, it is clear that models with very different spectra can have very similar photometry. *JWST* may also allow us to detect molecules that are not currently included in most models; for example, Shabram et al. (2011) showed that if species such as C_2H_2 and HCN exist in the atmosphere of GJ 436b, their abundances could be constrained by measuring the widths of features at 1.5, 3.3, and $7 \mu\text{m}$.

Greene et al. (2016) quantify our ability to constrain planet properties of a wider variety of atmospheres, including hot Jupiters, warm Neptunes, warm sub-Neptunes, and cool super-Earths, with *JWST*, and they find that the mixing ratios of major species in warm Neptunes like GJ 436b can be constrained to within better than 1 dex with a single secondary eclipse observation for each wavelength region from 1 to $11 \mu\text{m}$.

5.5. Measuring Internal Dissipation Factor Using T_{int}

Measuring T_{int} of GJ 436b using atmospheric models allows us to approximate the dissipation factor in GJ 436b’s interior, Q' . Q' is defined as $3Q/2k_2$, where Q is the quality factor and k_2 is the Love number of degree 2 (Goldreich & Soter 1966). Our best-fit T_{int} from the retrieval analysis is 336 K. Agúndez et al. (2014) calculated relations between T_{int} and Q' assuming obliquities of 0° and 15° and three different rotation speeds (1:1 resonance, 3:2 resonance, and pseudosynchronous). Assuming $T_{\text{int}} \sim 300\text{--}350$ K, their calculations suggest that $Q' \sim 2 \times 10^5\text{--}10^6$. These values are somewhat larger than the value of Q' that has been measured using Neptune’s satellites of between 3.3×10^4 and 1.35×10^5 (Zhang & Hamilton 2008).

If this high value for Q' is correct, this has significant implications for both the structure of GJ 436b itself and the evolution of the planetary system. In particular, a high Q' is consistent with a tidal circularization timescale that is longer than the age of the system, allowing GJ 436b to maintain its nonzero eccentricity ($e \sim 0.15$) without invoking another object in the system (Jackson et al. 2008; Batygin et al. 2009). This is consistent with the observations to date that have not found a third body in the GJ 436 system despite extensive searches (see Section 1.3). If GJ 436b’s Q does differ significantly from Neptune’s, this potentially implies a structural difference between hot Neptunes on short orbits and the ice giants in our own solar system.

5.6. Condensation of Graphite

As has been discussed in, e.g., Moses et al. (2013), cool, high-metallicity atmospheres may have regions that are stable for the condensation of graphite. Indeed, the very high metallicity models favored by the retrieval models do indeed cross the graphite stability curve above 0.1 bars. While the effect of this condensation is beyond the scope of this work, the major effects would be twofold. First, the graphite condensation will deplete the carbon reservoir, decreasing the CO abundance in the upper atmosphere. In addition, the condensed graphite may form into cloud particles with their own opacity. Like other clouds and hazes, graphite clouds would likely decrease the size of features in transmission spectra and thermal emission spectra and may either increase or decrease the albedo depending on the optical properties of the graphite particles.

5.7. Spatially Inhomogeneous Clouds

Planetary atmospheres are by their nature three-dimensional and complex, and clouds in these atmospheres may be nonuniformly located. In particular, the terminators of a planet have different circulation patterns and temperatures than the substellar point (e.g., Lewis et al. 2010; Kataria et al. 2016). It has recently been shown that nonuniform clouds on the terminators of planets will affect interpretation of transmission spectra (Line & Parmentier 2016). Furthermore, fitting the same one-dimensional model to both the thermal emission and transmission spectra may not be an accurate assumption. For example, the terminators may be cloudy while the thermal emission is dominated by a relatively cloud-free region. This effect should be investigated in the future, especially with higher-resolution and higher-S/N thermal emission and transmission spectra from *JWST*.

6. CONCLUSION

We have presented new observations of GJ 436b’s thermal emission at 3.6 and 4.5 μm , which are in agreement with previous analyses from Lanotte et al. (2014) and reduce the uncertainties of GJ 436b’s flux at those wavelengths. For the first time, we combine these revised data with *Spitzer* photometry from 5.6 to 16 μm and transmission spectra from *HST*/WFC3 and compare these data to both self-consistent and retrieval models. We vary the metallicity, internal temperature from tidal heating, disequilibrium chemistry, heat redistribution, and cloud properties. We find that our nominal best-fitting self-consistent models have 200–1000 \times solar metallicity, $T_{\text{int}} = 240$ K, $f_{\text{sed}} = 0.3\text{--}1$ sulfide/salt clouds, disequilibrium chemistry, and planet-wide average temperature profile, but this model does not provide an accurate fit to the observations. Retrieval models find a statistically better fit to the ensemble data than the self-consistent model, with parameters in general agreement with the self-consistent approach: all signs point to a high metallicity, with best fits above several hundred times solar metallicity, and tidal heating warming its interior, with best-fit $T_{\text{int}} \sim 300\text{--}350$ K. These results are consistent with results from interior models to match the mass and radius, with core masses around $10 M_{\oplus}$.

While Neptune has been measured, based on its methane abundance, to have an atmospheric carbon enhancement of $\sim 100\times$ solar, repeated observations of both the thermal emission and transmission spectra of the first exo-Neptune to be studied in detail, GJ 436b, have demonstrated that it likely

has a significantly higher metallicity. Neptune itself may actually be more enhanced in other elements than it is in carbon; Luszcz-Cook & de Pater (2013) infer a 400–600 \times solar enhancement in oxygen from microwave observations of upwelled CO in Neptune, though this cannot be verified with infrared spectra since oxygen is frozen into clouds. Studies of warmer exoplanet atmospheres will allow us to spectroscopically measure abundances of these molecules like oxygen that are locked into clouds in the cold ice giants of our solar system, potentially revealing unexpected patterns in the metal enrichments of these intermediate-mass objects.

An interesting new paradigm for this class of intermediate-sized planets is now being pieced together: we suggest that Neptune-mass planets may be more compositionally diverse than previously imagined. High-quality data across a range of Neptune-mass planets with different temperatures and host stars will be critical to investigate the diversity of this class of planets.

We thank the anonymous referee for their helpful suggestions. We also thank Konstantin Batygin and Greg Laughlin for helpful discussions that improved the paper. This work was performed in part under contract with the Jet Propulsion Laboratory (JPL) funded by NASA through the Sagan Fellowship Program executed by the NASA Exoplanet Science Institute. H.A.K. acknowledges support from the Sloan Foundation and from NASA through an award issued by JPL/Caltech. J.J.F. acknowledges Hubble grants HST-GO-13501.06-A and HST-GO-13665.004-A and NSF grant AST-1312545. M.S.M. acknowledges support from the NASA Origins program. M.R.L. acknowledges support provided by NASA through Hubble Fellowship grant no. 51362 awarded by the Space Telescope Science Institute, which is operated by the Association of Universities for Research in Astronomy, Inc., for NASA, under the contract NAS 5-26555. This work is based on observations made with the *Spitzer Space Telescope*, which is operated by the Jet Propulsion Laboratory, California Institute of Technology, under contract with NASA.

Software: CHIMERA (Line et al. 2012, 2013, 2014), CEA (Gordon et al. 1984), KINETICS (Allen et al. 1981; Yung et al. 1984; Moses et al. 2005), disort (Stamnes et al. 1988; Buras et al. 2011), PYMULTINEST (Buchner et al. 2014).

REFERENCES

- Ackerman, A. S., & Marley, M. S. 2001, *ApJ*, 556, 872
 Agúndez, M., Venot, O., Selsis, F., & Iro, N. 2014, *ApJ*, 781, 68
 Allen, M., Yung, Y. L., & Waters, J. W. 1981, *JGR*, 86, 3617
 Alonso, R., Barbieri, M., Rabus, M., et al. 2008, *A&A*, 487, L5
 Ballard, S., Chaplin, W. J., Charbonneau, D., et al. 2014, *ApJ*, 790, 12
 Ballard, S., Charbonneau, D., Deming, D., et al. 2010a, *PASP*, 122, 1341
 Ballard, S., Christiansen, J. L., Charbonneau, D., et al. 2010b, *ApJ*, 716, 1047
 Batygin, K., Laughlin, G., Meschiari, S., et al. 2009, *ApJ*, 699, 23
 Beaulieu, J.-P., Tinetti, G., Kipping, D. M., et al. 2011, *ApJ*, 731, 16
 Beust, H., Bonfils, X., Montagnier, G., Delfosse, X., & Forveille, T. 2012, *A&A*, 545, A88
 Buchner, J., Georgakakis, A., Nandra, K., et al. 2014, *A&A*, 564, A125
 Buras, R., Dowling, T., & Emde, C. 2011, *JQSR*, 112, 2028
 Burrows, A., Marley, M., Hubbard, W. B., et al. 1997, *ApJ*, 491, 856
 Burrows, A., & Sharp, C. M. 1999, *ApJ*, 512, 843
 Butler, R. P., Vogt, S. S., Marcy, G. W., et al. 2004, *ApJ*, 617, 580
 Cáceres, C., Ivanov, V. D., Minniti, D., et al. 2009, *A&A*, 507, 481
 Cahoy, K. L., Marley, M. S., & Fortney, J. J. 2010, *ApJ*, 724, 189
 Casewell, S. L., Lawrie, K. A., Maxted, P. F. L., et al. 2015, *MNRAS*, 447, 3218
 Deming, D., Harrington, J., Laughlin, G., et al. 2007, *ApJL*, 667, L199
 Deming, D., Knutson, H., Kammer, J., et al. 2015, *ApJ*, 805, 132

- Demory, B.-O., Gillon, M., Barman, T., et al. 2007, *A&A*, 475, 1125
- Feroz, F., Hobson, M. P., & Bridges, M. 2009, *MNRAS*, 398, 1601
- Fortney, J. J., Marley, M. S., & Barnes, J. W. 2007, *ApJ*, 659, 1661
- Fortney, J. J., Marley, M. S., Lodders, K., Saumon, D., & Freedman, R. 2005, *ApJL*, 627, L69
- Fortney, J. J., Marley, M. S., Saumon, D., & Lodders, K. 2008, *ApJ*, 683, 1104
- Fortney, J. J., Mordasini, C., Nettelmann, N., et al. 2013, *ApJ*, 775, 80
- Freedman, R. S., Lustig-Yaeger, J., Fortney, J. J., et al. 2014, *ApJS*, 214, 25
- Freedman, R. S., Marley, M. S., & Lodders, K. 2008, *ApJS*, 174, 504
- Gillon, M., Demory, B.-O., Barman, T., et al. 2007a, *A&A*, 471, L51
- Gillon, M., Pont, F., Demory, B.-O., et al. 2007b, *A&A*, 472, L13
- Goldreich, P., & Soter, S. 1966, *Icar*, 5, 375
- Gordon, S., & McBride, B. 1994, Computer Program for Calculation of Complex Chemical Equilibrium Compositions and Applications I. Analysis, NASA Technical Report, NASA RP-1311, <https://www.grc.nasa.gov/WWW/CEAWeb/RP-1311.htm>
- Gordon, S., & McBride, B. 1994, Computer Program for Calculation of Complex Chemical Equilibrium Compositions and Applications II. User's Manual and Program Description, NASA Technical Report, NASA RP-1311-P2, <https://www.grc.nasa.gov/WWW/CEAWeb/RP-1311P2.htm>
- Gordon, S., McBride, B., & Zeleznik, F. J. 1984, Computer Program for Calculation of Complex Chemical Equilibrium Compositions and Applications. Supplement 1: Transport Properties, NASA Technical Report, NASA-TM-86885
- Greene, T. P., Line, M. R., Montero, C., et al. 2016, *ApJ*, 817, 17
- Hu, R., Seager, S., & Yung, Y. L. 2015, *ApJ*, 807, 8
- Jackson, B., Greenberg, R., & Barnes, R. 2008, *ApJ*, 681, 1631
- Kammer, J. A., Knutson, H. A., Line, M. R., et al. 2015, *ApJ*, 810, 118
- Kataria, T., Sing, D. K., Lewis, N. K., et al. 2016, *ApJ*, 821, 9
- Knutson, H. A., Benneke, B., Deming, D., & Homeier, D. 2014a, *Natur*, 505, 66
- Knutson, H. A., Fulton, B. J., Montet, B. T., et al. 2014b, *ApJ*, 785, 126
- Knutson, H. A., Madhusudhan, N., Cowan, N. B., et al. 2011, *ApJ*, 735, 27
- Kreidberg, L., Line, M. R., Bean, J. L., et al. 2015, *ApJ*, 814, 66
- Lanotte, A. A., Gillon, M., Demory, B.-O., et al. 2014, *A&A*, 572, A73
- Lewis, N. K., Knutson, H. A., Showman, A. P., et al. 2013, *ApJ*, 766, 95
- Lewis, N. K., Showman, A. P., Fortney, J. J., et al. 2010, *ApJ*, 720, 344
- Line, M. R., Knutson, H., Wolf, A. S., & Yung, Y. L. 2014, *ApJ*, 783, 70
- Line, M. R., Liang, M. C., & Yung, Y. L. 2010, *ApJ*, 717, 496
- Line, M. R., & Parmentier, V. 2016, *ApJ*, 820, 78
- Line, M. R., Vasisht, G., Chen, P., Angerhausen, D., & Yung, Y. L. 2011, *ApJ*, 738, 32
- Line, M. R., Wolf, A. S., Zhang, X., et al. 2013, *ApJ*, 775, 137
- Line, M. R., & Yung, Y. L. 2013, *ApJ*, 779, 3
- Line, M. R., Zhang, X., Vasisht, G., et al. 2012, *ApJ*, 749, 93
- Luszcz-Cook, S. H., & de Pater, I. 2013, *Icar*, 222, 379
- Madhusudhan, N., & Seager, S. 2011, *ApJ*, 729, 41
- Mandel, K., & Agol, E. 2002, *ApJL*, 580, L171
- Maness, H. L., Marcy, G. W., Ford, E. B., et al. 2007, *PASP*, 119, 90
- Marley, M. S., Gelino, C., Stephens, D., Lunine, J. I., & Freedman, R. 1999, *ApJ*, 513, 879
- Marley, M. S., & McKay, C. P. 1999, *Icar*, 138, 268
- Marley, M. S., Saumon, D., Guillot, T., et al. 1996, *Sci*, 272, 1919
- Marley, M. S., Seager, S., Saumon, D., et al. 2002, *ApJ*, 568, 335
- McKay, C. P., Pollack, J. B., & Courtin, R. 1989, *Icar*, 80, 23
- Morello, G., Waldmann, I. P., Tinetti, G., et al. 2015, *ApJ*, 802, 117
- Morley, C. V., Fortney, J. J., Kempton, E. M.-R., et al. 2013, *ApJ*, 775, 33
- Morley, C. V., Fortney, J. J., Marley, M. S., et al. 2012, *ApJ*, 756, 172
- Morley, C. V., Fortney, J. J., Marley, M. S., et al. 2015, *ApJ*, 815, 110
- Moses, J. I., Fouchet, T., Bézard, B., et al. 2005, *JGRE*, 110, 8001
- Moses, J. I., Line, M. R., Visscher, C., et al. 2013, *ApJ*, 777, 34
- Moses, J. I., Visscher, C., Fortney, J. J., et al. 2011, *ApJ*, 737, 15
- Nettelmann, N., Kramm, U., Redmer, R., & Neuhäuser, R. 2010, *A&A*, 523, A26
- Pál, A., Bakos, G. Á., Torres, G., et al. 2010, *MNRAS*, 401, 2665
- Parmentier, V., & Guillot, T. 2014, *A&A*, 562, A133
- Pont, F., Gilliland, R. L., Knutson, H., Holman, M., & Charbonneau, D. 2009, *MNRAS*, 393, L6
- Ribas, I., Font-Ribera, A., & Beaulieu, J.-P. 2008, *ApJL*, 677, L59
- Saumon, D., Chabrier, G., & Horn, H. M. V. 1995, *ApJS*, 99, 713
- Saumon, D., & Marley, M. S. 2008, *ApJ*, 689, 1327
- Shabram, M., Fortney, J. J., Greene, T. P., & Freedman, R. S. 2011, *ApJ*, 727, 65
- Stammes, K., Tsay, S.-C., Jayaweera, K., & Wiscombe, W. 1988, *ApOpt*, 27, 2502
- Stevenson, K. B., Harrington, J., Lust, N. B., et al. 2012, *ApJ*, 755, 9
- Stevenson, K. B., Harrington, J., Nymeyer, S., et al. 2010, *Natur*, 464, 1161
- Sudarsky, D., Burrows, A., & Pinto, P. 2000, *ApJ*, 538, 885
- Thompson, S. L. 1990, ANEOS—Analytic Equations of State for Shock Physics Codes, Sandia Natl. Lab. Doc. SAND89-2951
- Thorngren, D. P., Fortney, J. J., Murray-Clay, R. A., & Lopez, E. D. 2016, *ApJ*, 831, 64
- Toon, O. B., McKay, C. P., Ackerman, T. P., & Santhanam, K. 1989, *JGR*, 94, 16287
- Toon, O. B., Pollack, J. B., & Sagan, C. 1977, *Icar*, 30, 663
- Visscher, C., Lodders, K., & Fegley, B., Jr. 2010, *ApJ*, 716, 1060
- von Braun, K., Boyajian, T. S., Kane, S. R., et al. 2012, *ApJ*, 753, 171
- Wong, I., Knutson, H. A., Lewis, N. K., et al. 2015, *ApJ*, 811, 122
- Yung, Y. L., Allen, M., & Pinto, J. P. 1984, *ApJS*, 55, 465
- Zahnle, K. J., & Marley, M. S. 2014, *ApJ*, 797, 41
- Zellem, R. T., Lewis, N. K., Knutson, H. A., et al. 2014, *ApJ*, 790, 53
- Zhang, K., & Hamilton, D. P. 2008, *Icar*, 193, 267